Journal of Orthopaedic Translation 31 (2021) 41–51

Contents lists available at ScienceDirect

Journal of Orthopaedic Translation

journal homepage: www.journals.elsevier.com/journal-of-orthopaedic-translation

PLGA/β-TCP composite scaffold incorporating cucurbitacin B promotes bone regeneration by inducing angiogenesis

Wen-Xiang Cheng [a,b,1], Yan-Zhi Liu [a,e,1], Xiang-Bo Meng [a], Zheng-Tan Zheng [a], Ling-Li Li [a], Li-Qing Ke [a], Ling Li [a], Cui-Shan Huang [a], Guo-Yuan Zhu [d], Hu-Dan Pan [d], Ling Qin [a,c], Xin-Luan Wang [a,c,*], Peng Zhang [a,b,**]

[a] Centre for Translational Medicine Research & Development, Shenzhen Institute of Advanced Technology, Chinese Academy of Sciences, Shenzhen, PR China
[b] Shenzhen Engineering Research Center for Medical Bioactive Materials, Shenzhen, PR China
[c] Musculoskeletal Research Laboratory, Department of Orthopaedics & Traumatology, The Chinese University of Hong Kong, Hong Kong
[d] State Key Laboratory of Quality Research in Chinese Medicine, Macau Institute for Applied Research in Medicine and Health, Macau University of Science and Technology, Macau, PR China
[e] Guangdong Key Laboratory for Research and Development of Natural Drugs, Marine Medical Research Institute, Guangdong Medical University, Zhanjiang, PR China

ARTICLE INFO

Keywords:
Biomaterials
Cucurbitacin B
Angiogenesis
Bone regeneration
3D printing

ABSTRACT

Objectives: Vascularization is an essential step in successful bone tissue engineering. The induction of angiogenesis in bone tissue engineering can be enhanced through the delivery of therapeutic agents that stimulate vessel and bone formation. In this study, we show that cucurbitacin B (CuB), a tetracyclic terpene derived from Cucurbitaceae family plants, facilitates the induction of angiogenesis *in vitro*.

Methods: We incorporated CuB into a biodegradable poly (lactide-co-glycolide) (PLGA) and β-tricalcium phosphate (β-TCP) biomaterial scaffold (PT/CuB) Using 3D low-temperature rapid prototyping (LT-RP) technology. A rat skull defect model was used to verify whether the drug-incorporated scaffold has the effects of angiogenesis and osteogenesis *in vivo* for the regeneration of bone defect. Cytotoxicity assay was performed to determine the safe dose range of the CuB. Tube formation assay and western blot assay were used to analyze the angiogenesis effect of CuB.

Results: PT/CuB scaffold possessed well-designed bio-mimic structure and improved mechanical properties. CuB was linear release from the composite scaffold without affecting pH value. The results demonstrated that the PT/CuB scaffold significantly enhanced neovascularization and bone regeneration in a rat critical size calvarial defect model compared to the scaffold implants without CuB. Furthermore, CuB stimulated angiogenic signaling via up-regulating VEGFR2 and VEGFR-related signaling pathways.

Conclusion: CuB can serve as promising candidate compound for promoting neovascularization and osteogenesis, especially in tissue engineering for repair of bone defects.

The translational potential of this article: This study highlights the potential use of CuB as a therapeutic agent and strongly support its adoption as a component of composite scaffolds for tissue-engineering of bone repair.

1. Introduction

Successful bone regeneration represents a major ongoing challenge in large segmental bone defect. Neovascularization is crucial to both intramembranous and endochondral bone formation during bone defect repairing [1]. Current tissue engineering strategies use an artificial biomaterial scaffold containing either biochemical stimuli, stem cells, or a combination of these treatments to establish regeneration [2], and in particular, to ensure vascularization and angiogenesis, which are essential for cell survival and tissue function [3]. Vascularization is a main

* Corresponding author. Translational Medicine R&D Center, Institute of Biomedical and Health Engineering, Shenzhen Institute of Advanced Technology, Chinese Academy of Sciences, Shenzhen, 518055, PR China.
** Corresponding author. Translational Medicine R&D Center, Institute of Biomedical and Health Engineering, Shenzhen Institute of Advanced Technology, Chinese Academy of Sciences, Shenzhen, 518055, PR China.
E-mail addresses: xl.wang@siat.ac.cn (X.-L. Wang), peng.zhang@siat.ac.cn (P. Zhang).
[1] These authors contributed equally as first author to this work.

https://doi.org/10.1016/j.jot.2021.10.002
Received 9 July 2021; Received in revised form 7 October 2021; Accepted 8 October 2021

challenge in successful bone tissue engineering. To stimulate vascularization and promote bone regeneration, bioactive factors can incorporate into the tissue regeneration scaffold [4]. Various growth factors such as VEGF, FGF, IGF, PDGF, etc. have shown effect in promoting neovascularization in the early stages of bone tissue repair [5,6]. However, concerns persist regarding its efficacy due to observations of poorly organized, leaky, and other side-effects [7].

Higher effective, lower toxic, more stable and less expensive components are huge unmet needs, even variety of products in bone tissue engineering (BTE). The natural medicinal compounds are stable and easy to obtain, which have been widely used in BTE. Cucurbitacin B, tetracyclic terpenes derived from Cucurbitaceae family plants, *e.g.,* squash, pumpkin, cucumber, and melons (Fig. 1A) [8]. This natural compound was be found in anti-cancer effect in non-small cell lung cancer, gastric cancer, breast cancer et al. Current studies have found that it mainly regulates STAT3/ROS/PI3K and related signal pathways [9,10]. Also, it has anti-inflammation effect, which can suppress gout arthritis [11]. Different from the research in above, scientists found its bioactivity which induces angiogenesis with safety dose [12]. Most of interestingly, our preliminary *in vitro* experiments revealed that CuB exhibited a substantial angiogenic effect at low and no-toxicity doses ($\leq$30 nM) in EA.hy926 cells, suggesting that this compound has strong therapeutic potential for treatment of tissue injuries, especially in bone regeneration.

Poly (lactide-co-glycolide) (PLGA) and β-tricalcium phosphate (β-TCP) have been used extensively in tissue engineering due to their high biocompatibility, already approved by FDA for several clinical applications [13,14]. In our previous work, we used the PLGA and β-TCP scaffold as a filler material and drug carrier in bone defects [2]. The scaffolds could provide osteoinductive effects, as well as a 3D architecture for host cell infiltration. The previous data provided the evidence of the proper proportion of PLGA and TCP could preserve the stable pH value [13], which benefited for ameliorating local microenvironment to contribute to cell growth. We incorporated CuB into the PLGA/β-TCP scaffold by 3D low-temperature rapid prototyping (LT-RP) technology in this study, in order to promote local angiogenesis better at the early stage of bone repair. The mechanical properties and release of CuB from scaffold have been studied. Then the rat calvarial defect model has been used to examine whether the drug-incorporated scaffold provided *in vivo* angiogenic or osteogenic effects towards the regeneration of bone. In addition, we investigated the underlying mechanism of its angiogenic properties and the coupled osteogenic effects.

2. Methods and materials

2.1. Cell culture

The human umbilical vein cell line EA.hy926 (ATCC, USA) was cultured in Dulbecco's modified Eagle medium (DMEM, Gibco, USA) supplemented with 10% fetal bovine serum (FBS, Gibco, USA). Human bone marrow-derived mesenchymal stem cells (hBMSC, Cyagen, China)

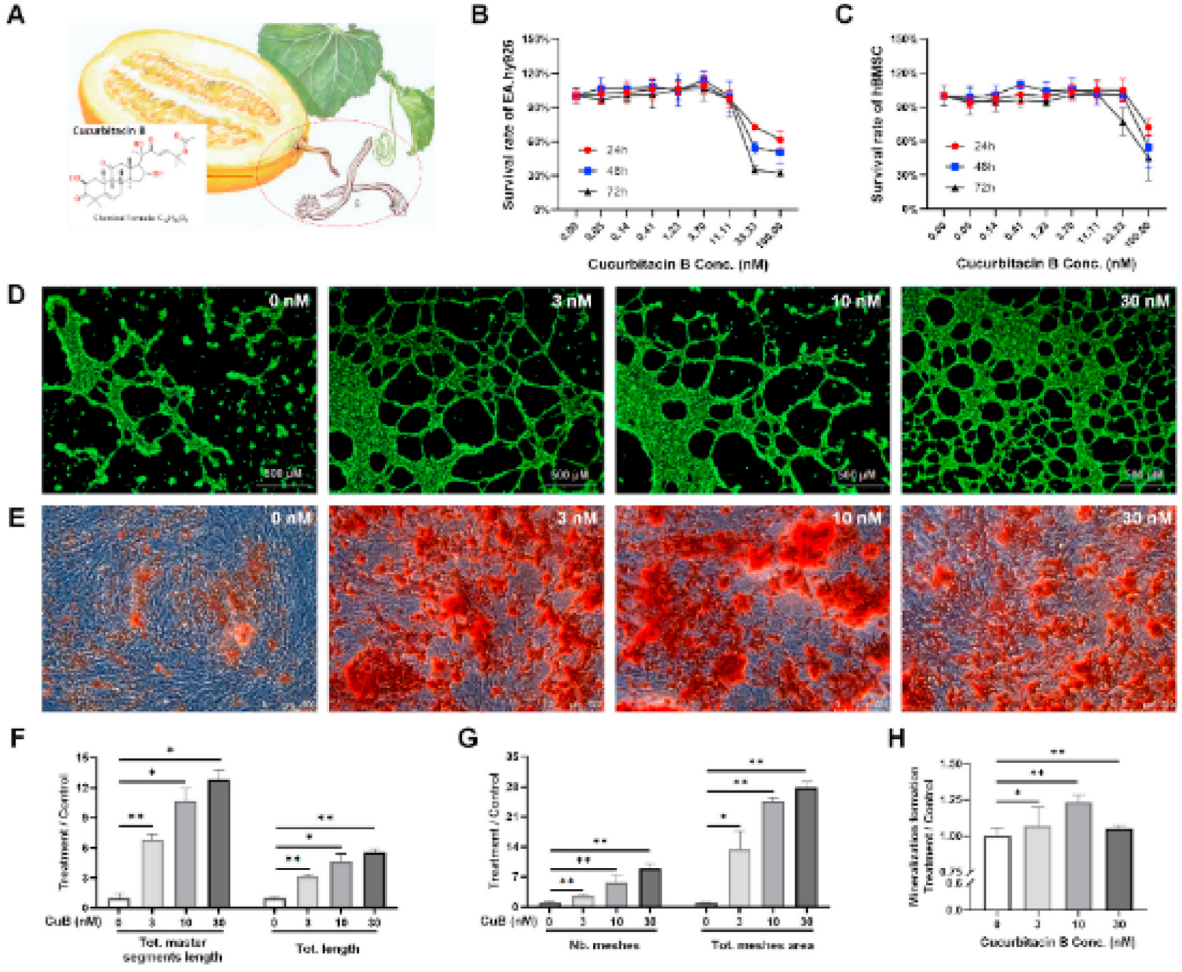

Figure 1. A. Picture of muskmelon, *Cucumis melo L* (dry muskmelon pedicel) and chemical structure of cucurbitacin B; B & C. Cytotoxity of CuB on EA.hy926 and hBMSC; D. The *in vitro* angiogenesis assay of EA.hy926 treated by CuB; E. The *in vitro* osteogenesis assay of hBMSC treated by CuB. F & G. The effects of CuB with different concentrations on total master segments length, total length, total meshes area and number of meshes (n = 5, *$p < 0.05$, **$p < 0.01$, treatment groups versus ctrl group); H. Quantitative analysis of mineralization formation (n = 3, *$p < 0.05$, **$p < 0.01$, treatment groups versus ctrl group).

were cultured in complete medium (Cyagen, China). hBMSCs below passage 6 were used for all *in vitro* experiments. Cells were incubated at 37 °C, 5% CO_2.

2.2. Cytotoxicity tests

A Cell Counting Kit-8 (CCK-8) assay (Dojindo, Japan) were used to measure the cytotoxicity of CuB on EA.hy926 and hBMSC cells according to manufacturer instructions. Cells were grown in 96-well plates at 5×10^3 cells/well for 24 h treated with Cucurbitacin B (CuB, Extrasynthese Genay, France) over a range of concentrations (0–100 nM with triple gradient dilution) for 24, 48, and 72 h, respectively. The absorbance at 450 nm was detected by a microplate reader (Thermo Fisher, USA).

2.3. Tube formation assay

EA.hy926 cells (1.2×10^5 cells/well, containing 0, 3, 10, 30 nM CuB) was seeded on Matrigel (Corning, USA)-coated 24-well plate for 12 h. Cells were labeled by Calcein AM (Corning, USA) in HBSS (Gibico, USA) and incubated plates for 30 min at 37 °C. Images were captured using a fluorescent microscope (Zeiss, Germany), then quantified using Angiogenesis Analyzer plugin of ImageJ software (NIH, USA).

2.4. Osteogenesis assay

hBMSC cells were seeded at a density of 2×10^5 cells in 24-well plate and cultured in osteogenic media (STEMCELL, Canada) supplemented with 0, 3, 10, or 30 nM of CuB for 14 days, respectively. For mineralization assays, the cells were fixed in 4% Paraformaldehyde (Sigma–Aldrich, USA) solution and then stained with Alizarin Red (AR, Sigma–Aldrich, USA). Stained mineralized nodules were visualized by an inverted microscope in bright field (Zeiss, Germany). AR was extracted by incubation in 10% cetylpyridinium chloride buffer (Sigma–Aldrich, USA), the absorbance of the samples was measured at 560 nm by the microplate reader (Thermo Fisher, USA).

2.5. Protein extraction and western blotting

EA.hy926 cells were treated with CuB with 0, 10, 30 nM for 1 h or 2 h respectively. The cells were then lysed with RIPA buffer (Thermo Scientific™, USA). Phospho-VEGF Receptor 2 (Tyr951, Tyr966, Tyr1059, Tyr1175) antibodies, total VEGFR2 antibody, phospho-Akt (Ser473), phospho-Src (Tyr416), phospho-FAK (Tyr397), phospho-p38 MAPK (Thr180/Tyr182), phospho-PLCγ1 (Ser1248), phospho-p44/42 MAPK (Thr202/Tyr204) and GAPDH were used as primary antibodies. The samples were incubated with corresponding anti-Rabbit HRP secondary antibodies. All the antibodies were supplied by Cell Signaling Technology, USA. Representative blots are shown and were repeated a minimum of three times. Representative blots were captured by Image LabTM (Bio-Rad Inc., USA).

2.6. PLGA/TCP/CuB scaffold fabrication and scanning electron microscopy (SEM) analysis

The PLGA (75:25, Institute of Biomaterials of Shandong, China) was dissolved in 1,4-dioxane (Aladdin, China) to form a 10% (w/v) homogeneous solution [15]. Then β-TCP (Shanghai Bio-lu Biomaterials Co., China) was mixed with PLGA solution by 1:4 mass ratio (w/w) [13]. CuB (1%, w/w) was added into the PLGA/β-TCP mixture then stirred evenly with a magnetic stirrer to form PLGA/β-TCP/CuB (PT/CuB) uniform liquid paste. The composite scaffolds were fabricated by a LT-RT 3D printing machine (CLRF-2000-II, Tsinghua University, China) under −30 °C. Then, the scaffolds were lyophilized in a freeze dryer for 24 h (Bo Yi Kang FD-1-50, China) under vacuum of 20–40 Pa pressure [16,17]. Pure PLGA/β-TCP (PT) scaffold was used as a comparison.

PT and PT/CuB composite scaffolds were cut by a sharp blade in the middle. A scanning electron microscope (Supra 55, Zeiss, Germany) was used to exam the morphology of the materials. The two scaffolds were coated with gold by sputter coater. The porous structure was scanned under 15 kV acceleration voltage.

2.7. Porosity measurement and mechanical testing

The average pore sizes of the PT/CuB and PT composite scaffolds were analyzed by SEM images through Image Pro Plus software (NIH, USA). Porosity measurement of PT/CuB and PT composite scaffolds were characterized using micro-CT (Skyscan1176, Bruker, Germany) with a spatial resolution of 20 mm. Meanwhile, porosity of scaffolds were measured with ethanol immersion method according to Archimedes' Principle in a specific gravity bottle (Hubbard, Hanil, Korea) [18].

The scaffolds with a shape of $10 \times 10 \times 10$ mm^3 were prepared for mechanical test. The compression strength and compressive modulus were tested by mechanical tester (Instron E3000, USA) with a 250 N load according to ISO 844:2014 (www.iso.org). The crosshead speed was set at 1 mm/min, and the load was applied until the scaffold cracked. Three samples per group were measured, and each test repeated twice.

2.8. Cell morphology and viability detection in the surface of scaffolds

To evaluate the cell morphology and viability on the scaffolds, hBMSC cells were seeded in the sterilized scaffolds for 3 days. Live/dead cells staining assay was performed (Thermo Scientific™, USA) according to the manufacturer's instructions. Live and dead cells were stained with Calcein AM or EthD-1, respectively. The labeled live and dead cells on scaffolds were viewed under the fluorescence microscope (Leica, Germany). We also observed the cells morphology on the scaffolds by SEM. Cultured cells for 3 days on the scaffolds, then cells were fixed by 4% paraformaldehyde and lyophilized in a freeze dryer. After coating with gold, attached cells on the scaffolds were observed by SEM (Supra 55, Zeiss, Germany).

2.9. Degradation of scaffolds

PT and PT/CuB scaffolds were immersed in PBS and incubated at 37 °C for 30 days. After rinsing scaffolds with distilled water, then scaffolds were dried until weight stabilization. Dry scaffolds were measured at each time point. The percentage of weight loss was calculated according to the following equation: Weight loss % = (W0 −Wt)/W0 × 100% (W0 is the initial dry weight of the scaffold and Wt is the dry weight of the scaffold after degradation). The pH value of degradation medium was measured by pH meter (Mettler Toledo).

2.10. In vitro CuB release and CuB bioactivity

PT/CuB scaffold was cut into 200 mg per sample and immersed in 5 mL PBS (0.1 M, pH 7.4, HyClone™, USA), incubated at 37 °C. The degradation medium was collected twice a week until 4 weeks and substituted by same volume of fresh PBS. The residual scaffolds were collected at 0-, 1-, 2-, 3-, and 4-week. The dried residual scaffolds were dissolved in dimethylformamide (Aladdin, China) for CuB determination. The content of released CuB in degradation medium and remained CuB in residual scaffolds have been detected by the high-performance liquid chromatography (HPLC, Shimadzu, Japan). The bioactivity of released CuB was detected by tube formation assay and osteogenesis assay as described in 2.3 and 2.4.

2.11. Rat critical size calvarial defect model

Thirty 3-month-old Wistar female rats were randomly divided into three groups. Rats were anaesthetized with isoflurane (2%, Ringpu, China) inhalation. A 15 mm long incision in the scalp along the sagittal

suture was made. Two 5 mm full-thickness craniotomy defects were trephined in the dorsal part of the parietal bone lateral to sagittal suture [19]. PT or PT/CuB scaffolds were placed to fill in the defect (Fig. 4A). The control group (Ctrl) did not receive any implants. The rats were euthanized 8 weeks after implantation, then the skull was harvested. The animals were housed under special pathogen-free conditions at the animal facility (Ethical approval number: SIAT-IRB-170814-YGS-ZP-A03 70). This animal study was approved by the Animal Ethics Committee of Chinese Academy of Sciences Shenzhen Institute of Advanced Technology.

2.12. Magnetic resonance imaging (MRI)

The blood flow of the calvarial defect was detected using 3.0 T magnetic resonance imaging (MRI) scanner (uMR790, United Imaging, China) [20]. The MRI image signal have been obtained by Gadolinium-Based Contrast Agents (Beijing Beilu Pharmaceutical Co., China) intravenous injection. MRI scanning were carried out on anaesthetized rats at 3-, 5-, and 7-week post-operation for each group (3 rats per group). The parameters of MRI scanning are as following: gradient-echo sequence [time to echo, 3.03 ms; repetition time, 7.12 ms; section thickness, 0.5 mm; imaging matrix = 160 × 90]. A total of 1200 dynamic images were obtained. Total thickness of the MRI scanning was analyzed to calculate the mean value describing the blood flow in defect areas.

2.13. Microfil perfusion

To investigate new blood vessels formation in defect area, microfil compound (Flowtech, USA) was perfused at 8-week post-operation. Rib cage was opened to expose the heart after animal anesthetized deeply. Heparinized normal saline 20 mL was perfused (100 U/ml, Aladdin, China) firstly, then microfil compound was slowly perfused. Perfused rats were stored at 4 °C overnight, then the calvaria was harvested and fixed in formalin [21].

2.14. Micro-CT analysis

Micro-CT was performed to analyse intrabony vascular formation. Microfil-injected samples were scanned after decalcification using Skyscan1176 Micro-CT scanner (Bruker, Germany) at 50 kV, 100 μA, 0.9 μm resolution, 0.5-degree rotation step settings, with 0.5 Al filter. For the analysis of bone formation within the defects, the harvested calvaria samples were fixed in formalin, and scanned using Skyscan1176 Micro-CT scanner with 16.4 μm resolution, at 70 kV, 114 μA, 0.6-degree rotation step settings, without any filter. A 5.0 mm-round centered on the defect was identified as region of interest (ROI). Then 3D reconstruction and quantitative analyses were performed using manufacturer's software (CTan, Bruker, Germany). PT scaffold was scanned to get the background to calculate the bone volume in bone defect areas.

2.15. Histology and immunohistochemistry

The cranial defect samples were fixed in 4% paraformaldehyde solution, then decalcified in EDTA-Decalcifying-fluid (Boster, China) and embedded in paraffin. Hematoxylin and eosin (H&E, Sigma–Aldrich, USA) staining was performed according to the manufacturer's protocol. Immunohistochemistry was performed with antibodies against VEGFA (Abcam, UK) and HIF-1α (Proteintech, China).

2.16. Goldner's trichrome staining

Goldner's trichrome staining was performed to distinguish osteoid, bone marrow and bone tissue. Each biopsy was fixed in 4% paraformaldehyde solution, dehydrated in a graded series of alcohol, and embedded in methylmethacrylate (Aladdin, China) for Goldner's trichrome staining (Leagene, China) as following the manufacturer's protocols. The slides were imaged using an inverted microscope (Leica, Germany).

2.17. Statistical analysis

All results are presented as average ± standard deviation. Differences between experimental groups was performed one-way ANOVA and Dunnett's test using SPSS (version 21.0, USA). All p values were two-tailed and $p < 0.05$ was considered statistically significant.

3. Results and discussion

3.1. Low dose of CuB promoted angiogenesis and osteogenesis process in vitro

3.1.1. Safety dosage determination

Many literatures reported the drug effect in the cell death dosage. It has been found that at high doses of CuB could induce cell-cycle arrest, apoptosis, and growth suppression of cancer cells [22]. The study reported that CuB inhibited angiogenesis at the 100 nM [23], which is the cytotoxic dosage. Recently, a drug screening result showed that CuB had broad cellular specificity, which could induce angiogenesis and protects cardiomyocytes against apoptosis in the no-cytotoxic dose [12].

In this study, we studied the effect of CuB in no-cytotoxic dose. To determine the margin of safety range for CuB dosages, we performed cytotoxicity assay in human umbilical vein cell line EA.hy926 and human bone marrow stem cells (hBMSC). A 34.9% and 76.9% cell survival rate was observed at 72 h of exposure to concentrations of ≤33.33 nM CuB for EA.hy926 (Fig. 1B) and hBMSC (Fig. 1C) cells, whereas most cells were killed at ≥100 nM CuB. Meanwhile, we performed live-dead cells staining at 72 h to observe the cell viability. The data showed that the number of cells were reduced, but cell viability was well in the 33.33 nM both in EA.hy926 and hBMSC cells, Therefore, the results indicated that 30 nM CuB might affect cell proliferation, but didn't affect the biological function of cells (Supplementary materials Figure S1). Since no cytotoxicity was observed when cells were exposured to 33.33 nM CuB, we selected this dosage or lower (≤30 nM) for *in vitro* angiogenesis and osteogenesis assays.

3.1.2. CuB promotes angiogenesis process in vitro

To explore the effects of CuB on angiogenesis *in vitro,* we first performed tube formation assays. We observed that vascular morphogenesis was initiated and multicellular tubular networks formed after 12 h of exposure to CuB in EA.hy926. Tube formation gradually increased in a dose-dependent manner (Fig. 1D). The major branch length (Fig. 1F) and total mesh (Fig. 1G) area both doubled at 30 nM, compared to untreated EA.hy926 cells. Between 3 and 30 nM CuB, the number of nodes, segments, and total segment lengths increased significantly over that of untreated cells, indicating substantially greater tubular network formation. Furthermore, compared with untreated groups, the 30 nM CuB treatments led to 12.8-fold and 5.5-fold higher numbers of total master segments and total length, respectively. The number of meshes and total mesh areas also significantly increased 9-fold and 28-fold, respectively, compared to the untreated group (Fig. 1F and G). These results indicated that ≤30 nM CuB enhanced tubulogenesis in EA.hy926 cells.

3.1.3. CuB promotes osteogenesis process in vitro

To detect mineralization potentially induced in response to CuB treatment, monolayer cultures were stained with AR at day 14 after CuB treatment. AR staining positive coloration of BMSCs cultured in osteogenic induction medium, plus or minus CuB, was generally more intense in cells supplemented with CuB, with significantly greater numbers of calcium nodules in 3 nM and 10 nM CuB treatment groups than in the control group (Fig. 1E and H). ALP activity was increased by CuB in a dose dependent manner after 3 days treatment. Realtime qPCR results

showed that CuB promoted the expression of ALP and OPN genes (Supplementary materials Figure S2). These results suggested that early osteoblast differentiation of hBMSCs was promoted by low doses of CuB. *In vitro* mineralization assays revealed that calcium phosphate deposition was greater in cells cultured in osteogenic induction medium containing CuB.

3.2. Morphology and in vitro degradation of the PT/CuB scaffold

3.2.1. Physical and chemical properties of scaffolds

We developed a porous drug-loaded composite scaffold. PLGA was used to recruit BMSCs and induce osteogenic differentiation [24,25], β-TCP provided appropriate mechanical strength [24], and, we hypothesized, CuB could potentially stimulate angiogenesis *in vivo*. We previously validated the porosity and apparent physical and mechanical properties of PLGA/β-TCP, and found that a PLGA:TCP mass ratio of 4:1 maintained a consistent pH 5–7 range throughout the *in vitro* degradation assays. PLGA produces acidic products, which can be neutralized with the alkaline products of TCP. Meanwhile, TCP could increase the strength of scaffold [13]. In this design, the PLGA/β-TCP (PT) scaffolds were loaded with or without 1.0% w/v (weight/volume percentage concentration) CuB. All scaffolds were fabricated uniformly ($20 \times 20 \times 20\ mm^3$) with regular macropores (Fig. 2A) by low temperature 3D printing. No differences were observable between scaffolds that contained CuB and those that did not.

Appropriate pore size is conducive to the differentiation, proliferation, and migration of mesenchymal stem cells and osteoblasts, as well as angiogenesis in local tissues [26]. For capillary neovascularization and new bone formation, the pore size of scaffolds is usually larger than 300 μm [27]. Macropore sizes typically ranged from 465 to 485 μm. Porosity and the mechanical properties of scaffolds are listed in Table 1. Given the contributions of pore size, porosity, and surface architecture to the effectiveness of a scaffold in regeneration, we considered that the scaffolds have the biomimetic structure. Then we used SEM microscopy to scrutinize the surface morphology. The SEM images showed that the macropores were smooth and that scaffold pores were highly interconnected in PT and PT/CuB scaffolds (Fig. 2B). We then seeded rat hBMSCs on the PT and PT/CuB scaffolds and cultured them in medium for three days, until they attached to spread into the scaffolds (Fig. 2C). Live/dead cell staining showed that cells grew well and successfully adhered to the surfaces of both PT and PT/CuB scaffolds (Fig. 2D). These results suggested that the scaffolds had good physical property. That could facilitate cell seeding and adhering, also might allow tissue ingrowth.

Table 1
Physicochemical properties of scaffolds ($\overline{X}$±SD).

Group (n = 6)	PT	PT/CuB
Macropore size (μm)	484.25 ± 20.02	465.17 ± 15.89
Porosity by micro-CT (%)	62.03 ± 1.78	65.59 ± 3.35
Porosity by ethanol immersion (%)	69.29 ± 3.90	70.92 ± 2.50
Young's Modulus (MPa)	26.08 ± 2.37	24.70 ± 3.90
Compressive Strength (MPa)	1.35 ± 0.15	1.28 ± 0.19

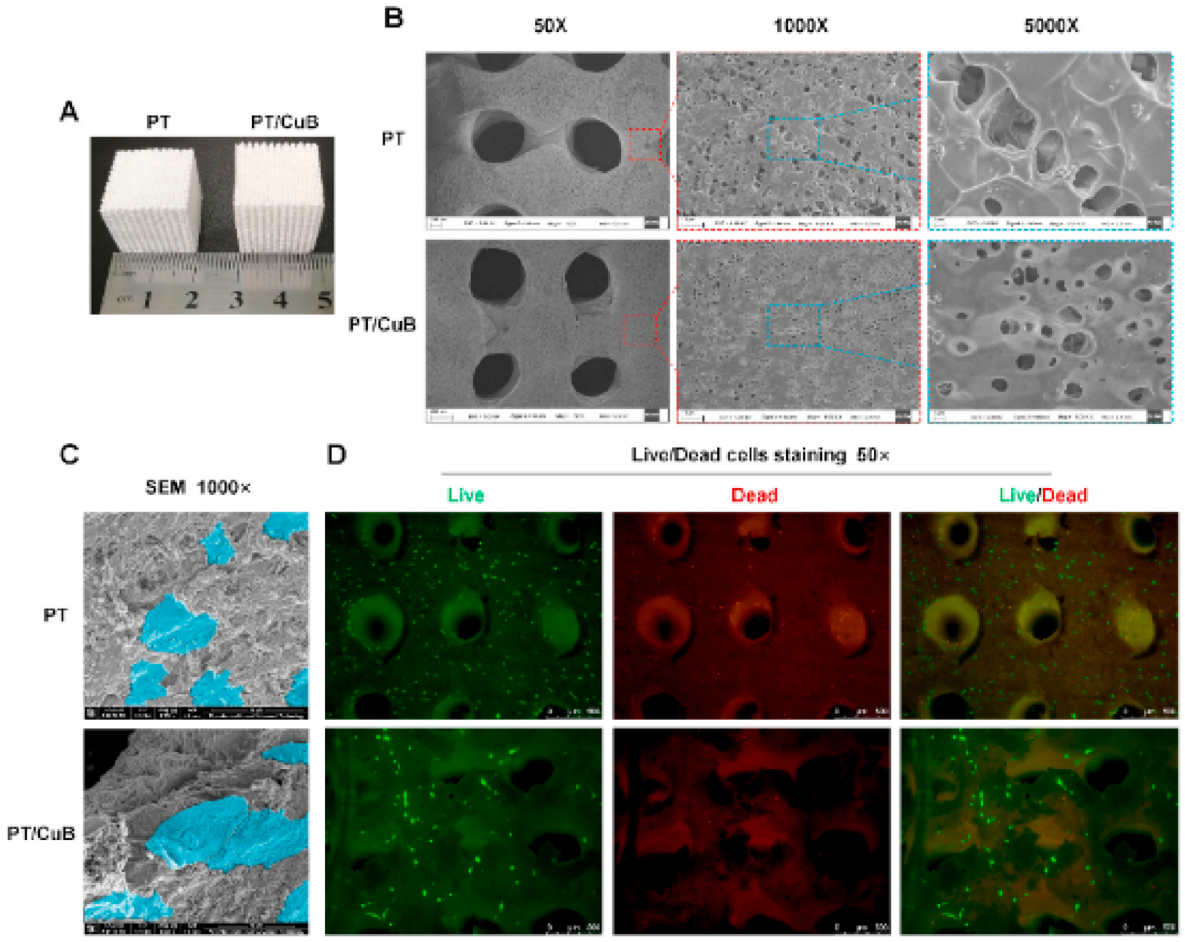

Figure 2. A. Gross appearance of PT and PT/CuB scaffolds; B. The SEM scanning of the scaffolds; C. hBMSCs morphologies on the scaffolds by SEM scanning (cells colored blue); D. Live (stained by Calcein AM, green) and dead (stained by Ethidium homodimer-1, red) cells staining images; merged images were showed on the right of figure. (For interpretation of the references to colour in this figure legend, the reader is referred to the Web version of this article.)

3.2.2. Scaffolds degradation and in vitro release of CuB

Since angiogenesis is an early event (about 4 weeks) in tissue repair, CuB release therefore needs to be measured over a 30-day period. To this end, we conducted *in vitro* degradation analysis in phosphate buffer saline (PBS, pH 7.27.4). The results showed that the weights of the PT and PT/CuB scaffolds decreased by 2.0% and 2.2% after 30 days of degradation, respectively (Fig. 3A). pH of repair tissue fluids may play a regulatory role in the healing and mineralization of bone. It was reported that bone repair tissue within first week after trauma, had a pH lower than normal serum [28]. Low tissue pH and locally acidic environments develops at bone fracture sites, result in hypoxic or ischemic conditions [29]. The pH value was slight decreased to 7.0 and 6.9 in PT/CuB and PT groups at day 3, respectively. Then pH values were back to around 7.2 and stable in degradation medium until 4 weeks. The pH value of PT and PT/CuB scaffold was alkaline and stable for the first four weeks (Fig. 3B), which benefited for ameliorating local microenvironment to contribute to cell growth. Notably, neither the loss of weight by PT and PT/CuB scaffolds, nor the change in pH of the medium were significantly different among any timepoints during the degradation period.

Theoretically, containing 1% of CuB (w/w) scaffold has been prepared by LT-RT 3D printing. We then examined the release of CuB over the degradation period. The results showed that CuB was released from the PT/CuB scaffold into degradation medium at a sustained rate of 1.70% per day (Fig. 3C), consistent with a linear decrease in residual

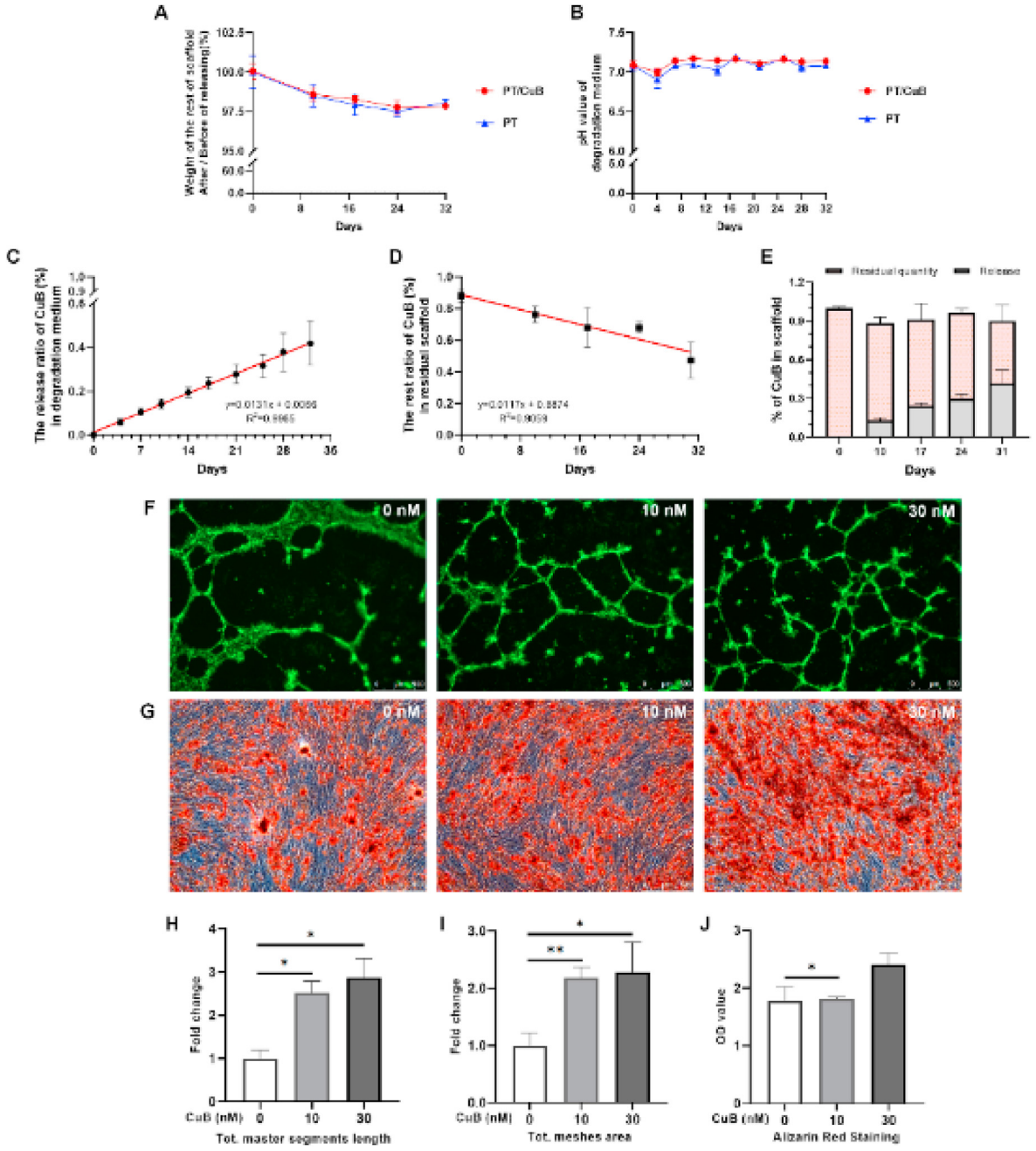

Figure 3. A. Weight of scaffolds after degradation; B. pH value in the degradation medium; C.The released ratio of CuB in degradation medium; D. The rest ratio of CuB in residual PT/CuB scaffold; E. The accumulated content of CuB in PT/CuB scaffold degradation medium and the residual PT/CuB scaffold; F. The tube formation of EA.hy926 cells which were treated by CuB from PT/CuB scaffold degradation medium. G. AR staining images which hBMSCs were treated by CuB from PT/CuB scaffold degradation medium; H & I. The effects on total master segments length and total meshes area treated by CuB from PT/CuB scaffold degradation medium (*$p < 0.05$, **$p < 0.01$, n = 5); J. Quantitative analysis of mineralization formation (*$p < 0.05$, **$p < 0.01$, n = 3).

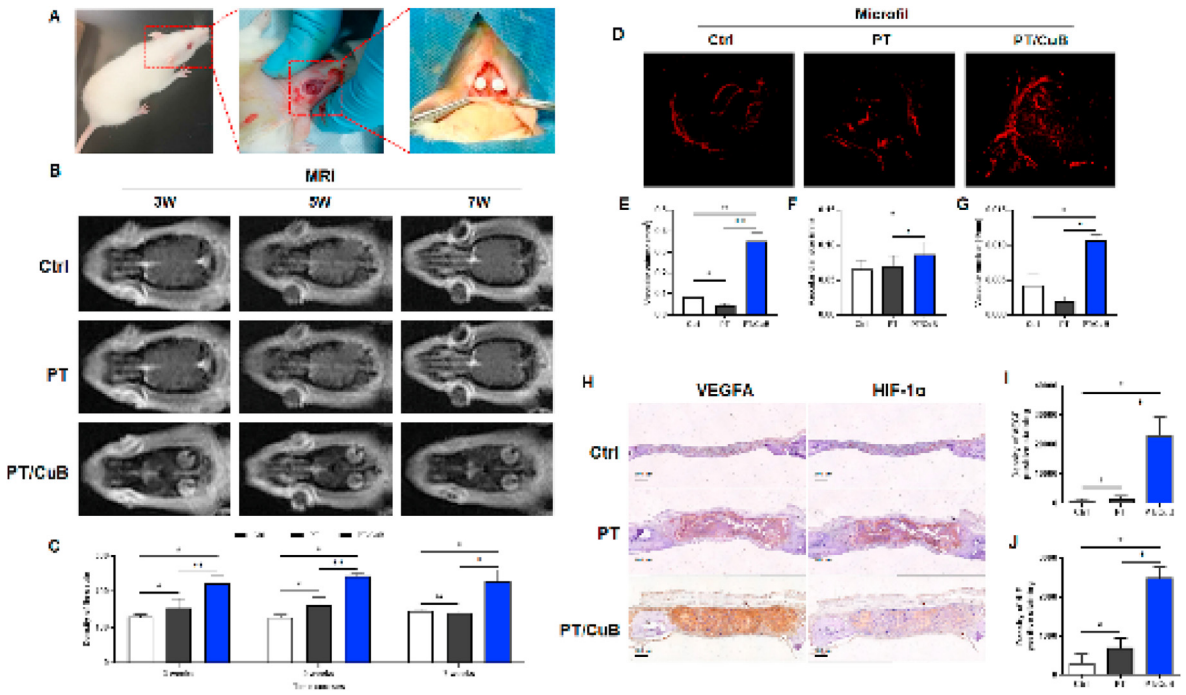

Figure 4. A. Operation of rat calvarial defect animal model; B. MRI scanning; C. Density of blood flow rate in rat calvarial defect area; D. Representative micro-CT images of vascularization at the defects at 8 weeks; E-G. The vascular volume, diameter, and number in rat calvarial defect area; H. VEGFA and HIF-1α IHC staining of rat calvarial at 8 weeks post-implantation; I. Density analysis of VEGFA expression; J. Density analysis of HIF-1α expression.
* PT/CuB groups versus PT group, n = 6, $*p < 0.05$, $**p < 0.01$.
# PT or PT/CuB groups versus sham group, n = 6, $\#p < 0.05$, $\#\#p < 0.01$.

drug levels in the scaffold (Fig. 3D). Near 0.9% of CuB from the PT/CuB scaffold has been detected together in degradation medium of PT/CuB scaffolds and residual scaffolds (Fig. 3E, Supplementary Table S1). These data indicated that CuB might be simply deposited by immersion in the scaffold rather than bound to the scaffold. In this study, we implanted 5 mm diameter, 1 mm thickness scaffold, the weight was 12.5 mg, containing 0.125 mg CuB. Based on our *in vitro* degradation results, the dose of CuB was around 6 μg/kg. And this concentration is under the safety dosage, which was 0.1 mg/kg intravenously or by oral gavage at 2–4 mg/kg in rats [30]. However, *in vivo* environment was complicated. Tissue kinetics and route of excretion are also need be investigated in the further study.

After confirming the stability of the scaffolds and CuB release in degradation medium, we then validated the biological activity of the released CuB from the PT/CuB scaffold using tube formation and osteogenesis assays. The results indicated that the release of CuB into the degradation medium resulted significant enhancement of angiogenesis (Fig. 3F, H and 3I) and osteogenesis *in vitro* (Fig. 3G and J), which was consistent with experiments using CuB without the scaffold for delivery (Fig. 1D and E). Taken together, these findings suggest that incorporated CuB could be released from biodegradable scaffold. Moreover, released CuB of PT/CuB scaffold still has biological activity, and thereby PT/CuB scaffold has potential applications to improve revascularization in bone tissue engineering.

3.3. CuB loaded scaffold promoting neovascularization in rat cranial defect animal model

Having confirmed that CuB has angiogenic and osteogenic effects *in vitro*, we next investigated whether the PT/CuB scaffold could enhance angiogenic and osteogenic function *in vivo* using a rat critical size calvarial defect model. To this end we created round 5 mm diameter defects in the skulls of rats. PT and PT/CuB scaffolds were implanted in the defects and un-implanted defects served as controls (Ctrl) (Fig. 4A, Supplementary materials Figure S3). Angiogenesis was measured at 3, 5, and 7 weeks by MRI analysis, which showed that the cranial defect sites were well-vascularized in both PT and PT/CuB groups, compared to those of the Ctrl group (Fig. 4B). Over the experimental time course, blood flow to the defect region continually increased, peaking at 5 weeks in the PT/CuB group. At 5 weeks, the blood flow was 1.89- and 1.3-fold greater in the PT/CuB group compared to the PT and Ctrl groups, respectively. By 7 weeks, the vascularization did not appear to increase in the PT/CuB group over that of 5 weeks but remained significantly greater than vascularization in the PT and Ctrl groups (Fig. 4C). By contrast un-implanted defects in the Ctrl rats failed to show any quantifiable difference in blood flow. These results indicated that the PT/CuB scaffold improved angiogenesis in the early stage of bone regeneration *in vivo*.

At 8 weeks, blood perfusion was performed on rats from each experimental group. We harvest the biopsies and conducted microCT-based angiography analysis to observe the newly formed vessels in the defect regions. The 3D imaging results showed a higher degree of neovascularization within the bone defect regions implanted with PT/CuB scaffolds compared to those with PT scaffolds (Fig. 4D). In addition, average vessel volume (Fig. 4E), vessel diameter (Fig. 4F), and vessel number (Fig. 4G) were all significantly greater in the PT/CuB group compared with the PT and Ctrl groups, $p < 0.05$. The results of these experiments supported our hypothesis that CuB supplementation to the PT scaffold could enhance angiogenesis during bone healing.

We further examined the effects of CuB using immunohistochemistry to observe expression of the angiogenic transcriptional activator HIF-1α and its downstream target VEGF *in situ* during the development of new vessels. Here, we observed that VEGF was strongly expressed in the bone defect region of the PT/CuB group, while, as expected, bone defects in the PT group showed substantially less positive staining and Ctrl defects were negative (Fig. 4H, left). Similarly, HIF-1α was clearly observable in explants of the PT/CuB group, exhibiting brighter staining than in the PT and Ctrl groups (Fig. 4H, right). Quantitative image analysis and statistical comparison of the explants confirmed that both VEGF and HIF-1α

were expressed at significantly higher levels in the PT/CuB group *in vivo* than the other groups (Fig. 4I and J). These findings were in consist with MRI and microCT imaging that indicated CuB doping of the PT scaffold led to significantly faster neovascularization than application of the scaffold alone. HIF-1α and VEGF play central roles in regulating cell metabolism for angiogenesis and subsequent bone formation [31,32]. Our results strongly implied that CuB enhances angiogenesis via up-regulated expression of HIF-1α and VEGF. These proteins have been shown to participate in the recruitment of endothelial and osteoprogenitor cells to bone defects for new vessel and bone formation [33].

3.4. CuB loaded scaffold enhanced the bone regeneration in a critical-size calvarial defect

Having determined that the PT/CuB scaffold enhanced *in vivo* angiogenesis, we then assessed whether the presence of CuB also facilitated faster bone formation. Using the same experimental design as that of *in vivo* angiogenesis assays, we then used micro-CT scanning to analyze the 5 mm cores at the centre of each defect at 8 weeks after implant to determine the volume of new bone tissue. The reconstructed 3D images showed that the PT/CuB scaffold induced a significantly higher amount of new bone formation than that of all other groups ($p < 0.05$) (Fig. 5A). Quantification by image analysis and statistical comparison showed that bone mineral density (BMD) and bone volume (BV) were both significantly higher in the PT/CuB group compared with the PT and Ctrl groups (Fig. 5B and C, respectively). However, we observed that the number of trabeculae (Tb. N) in the PT group was greater than that in the PT/CuB rats (Fig. 5D). Blood vessels and bone formation are coupled, so that osteogenesis and vasculogenesis occur together [34]. Together with the observed increase in vessel formation (Fig. 4), these results showed that CuB administration led to faster healing of bone injury than scaffold implants alone.

In histological observations, H&E and Goldner's staining both showed that in the PT/CuB and PT groups, osteoid accumulation was clearly observable in the defect sites, but only fibrous tissue was observed in the Ctrl group (Fig. 5E and F). Furthermore, local CuB release increased bone volume significantly compared to that in the PT group (Fig. 5F). These histomorphometric observations thus revealed that the PT scaffold was necessary to promote connective tissue closure of the bone injury, and that CuB application significantly improved the rate of bone regeneration compared to that of the scaffold alone. One study indicated that HIF-1α was a pro-osteogenic factor for woven bone formation after damaging loading [31]. Recent studies have shown that bone and vascular has important crosstalk and promote bone vasculature might inhibit bone loss [35]. Together with our result, PT/CuB scaffold might induce the new blood vessel formation through released CuB from composite scaffold. Chondrocytes and osteogenesis-related cells rely on the HIF-1α, which was produced by PT/CuB induced neovascularization. Then the cells were recruited on the scaffold allowing the coupling of angiogenesis and osteogenesis during bone regeneration in cranial defect. In the follow-up study, we will use the long bone defect animal model, extend the observation period, and further evaluate the angiogenic and osteogenic efficiency of PT/CuB scaffold in long bone defect repair.

3.5. CuB promote the angiogenesis via VEGFR2 signaling pathway

As CuB has shown great efficacy in angiogenesis *in vitro* and *in vivo,* we next investigated the molecular mechanisms through which CuB may contribute these apparently angiogenic effects. VEGFR proteins play a key role in survival, migration, and differentiation of endothelial cells, and also participate in the regulation of vascular permeability [36]. VEGFR2 signaling is necessary for ligand-stimulated proliferation, chemotaxis, and sprouting, as well as for survival of endothelial cells *in vitro* and angiogenesis *in vivo* [37]. Major VEGFR2 autophosphorylation sites located in the kinase insert domain (Tyr951/996) and the tyrosine kinase catalytic domain (Tyr1054/1059), in addition to Tyr1175 in the C-terminal tail [36,38]. We examined VEGFR2 for kinase activation by Western blotting to determine whether CuB induced autophosphorylation in EA.hy926 cells. The results showed that treatment with 10 nM CuB led to phosphorylation of the Tyr 996 site within 1 h, and slightly up-regulated phosphorylation of Tyr 1175 within 2 h. However, two other phosphorylation sites, Tyr 951 and Tyr 1059, remained undetectable (Fig. 6A and B). These results suggested that VEGFR2 was largely activated by CuB exposure via Tyr 996 autophosphorylation. Interestingly, heatmap visualization showed that lower doses of CuB may have induced greater up-regulation of the VEGFR2 pathway than the higher doses (Fig. 6K).

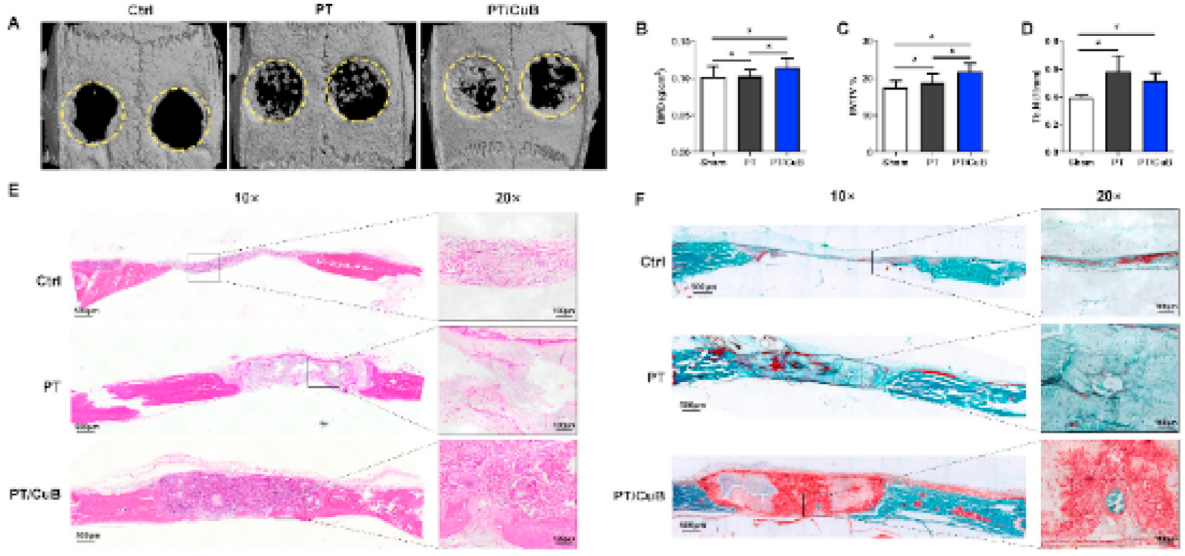

Figure 5. A. Micro-CT characterization of the rat calvarial defect area at 8 weeks post-implantation; B. The bone mineral density in rat calvarial defect area; C. BV/TV % in rat calvarial defect area; D. The number of trabeculae in rat calvarial defect area; E. HE staining of rat calvarial at 8 weeks post-implantation; F. Goldner's Trichrome image overview of rat calvarial defect area.
* PT/CuB groups versus PT group, n = 14, *$p < 0.05$, **$p < 0.01$.
# PT, PT/CuB groups versus sham group, n = 14, #$p < 0.05$, ##$p < 0.01$.

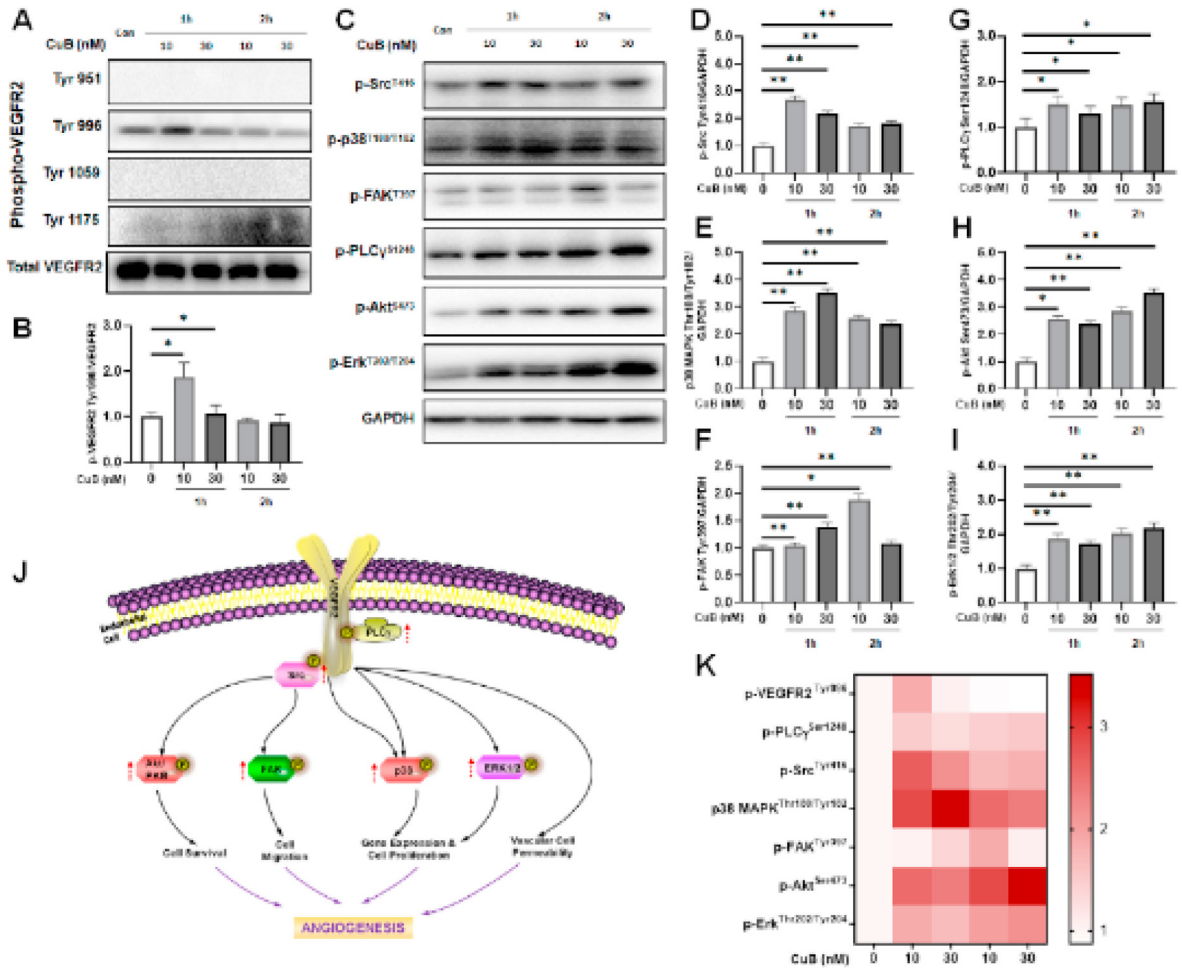

Figure 6. A&B. The effect of CuB regulated VEGFR2 phosphorylation and semi quantitative results (compared with control group, $*p < 0.05$, $**p < 0.01$, n = 3); C. Effect of CuB on the expression level of phosphorylated protein in angiogenesis signaling pathway; D-I. Semi quantitative results of Fig. 5C (compared with control group, $*p < 0.05$, $**p < 0.01$, n = 3); J. CuB promotes angiogenesis via VEGFR2 signalling pathway. K. Heat map comparisons of phosphor protein expression of key moleculars in VEGFR signalling pathway.

Activated VEGFR2 in endothelial cells elicits downstream phosphorylation of serine/threonine kinase Akt, PLCγ1, the Src family tyrosine kinases (Src), focal adhesion kinase (FAK), extracellular signal-regulated kinase (Erk), and the p38 mitogen-activated protein kinase (p38) [39] (Fig. 6J). Src kinases regulated cellular morphology, cell migration and polarization, as well as endothelial junctions and vascular barrier function [40,41]; FAK was found to be phosphorylated *in vitro* by Src [42]. Using Western blots, we observed that CuB increased p-38 and p-Src activation rapidly, within 1 h after treatment, while 2 h of exposure to 10 nM CuB led to a 1.9-fold up-regulation of p-FAK over that of the 30 nM treatment. Our results therefore indicated that p-Src was activated first, which subsequently phosphorylated p-FAK Tyr 576 after 2 h of CuB treatment (Fig. 6C–F).

Akt plays a critical role in endothelial cell survival [43], while PLCγ mediates activation of the Erk pathway required for proliferation of endothelial cells [41]. We further found that p-PLCγ accumulation increased ~2-fold under all CuB dosages at both 1 and 2 h after treatment, thus indicating continuous activation in the presence of CuB, whereas p-Akt and p-erk1/2 were dramatically up-regulated 3.2- and 2.1-fold, respectively, higher than untreated cells after 2 h of exposure to 30 nM CuB (Figure 6C and 6D-I). Erk and Akt were therefore significantly activated via PLCγ phosphorylation after CuB treatment for 2 h. CuB may thus promote vascular endothelial cell survival and proliferation via Akt and Erk signaling, which regulate the vasomotion and barrier function of vessels. Collectively, these data show that CuB activates VEGFR2 signaling to promote angiogenesis. Specifically, p38 and Src appear to be activated first in response to CuB, which then phosphorylate pFAK, while phosphorylation of p-PLCγ leads to downstream activation of p-Akt and p-erk1/2 (Fig. 6J and K).

Lack of sufficient vascularization at the bone defect site is one of the most important challenges in bone tissue engineering (BTE). The incorporation of angiogenic, osteogenic, and/or anti-inflammatory elements to enhance the pro-osteogenic properties of implant biomaterials has been a long-term objective for innovation in bone regeneration strategies [44,45]. The field of BTE has made considerable strides in recent decades towards advancing scaffold design and architecture [46]. Other long-standing challenges necessary for improvement of scaffold effectiveness in bone and vascular regeneration include prolonging the stability of encapsulated proteins during sustained release, and successful delivery of drugs and biomolecules from the biodegradable scaffold [47].

4. Conclusion

Taken as a whole, our data indicate that CuB, in low doses, can act as an agonist of VEGFR2 and subsequently promote angiogenesis via positive regulation of endothelial cell survival and proliferation, and may also affect cell migration and polarization. Additionally, the incorporation of CuB into a porous PLGA/β-TCP scaffold enhanced neovascularization and

bone regeneration *in vivo* in a rat calvarial critical-sized bone defect model. These results highlight the potential use of CuB as a therapeutic agent and strongly support its adoption as a component of composite scaffolds for tissue-engineering of bone repair.

Authorship

Conception and design of study: Xinluan Wang, Peng Zhang; Acquisition of data: Wenxiang Cheng, Yanzhi Liu, Xiangbo Meng, Zhengtan Zheng, Analysis and/or interpretation of data: Lingli Li, Liqing Ke, Cuishan Huang, Ling lIu, Drafting the manuscript: Wenxiang Cheng, Yanzhi Liu, Revising the manuscript critically for important intellectual content: Ling Qin, Xinluan Wang, Peng Zhang, Guoyuan Zhu; Hudan Pan, Approval of the version of the manuscript to be published (the names of all authors must be listed): Wenxiang Cheng, Yanzhi Liu, Xiangbo Meng, Zhengtan Zheng, Lingli Li, Liqing Ke, Ling Li, Cuishan Huang, Guoyuan Zhu, Hudan Pan, Ling Qin, Xinluan Wang, Peng Zhang.

Declaration of competing interest

There is no conflict of interest to declare.

Acknowledgements

The authors wish to express their gratitude to the financial supports from the National Key R&D Program of China (2018YFC1705205); Foreign cooperation project of Chinese Academy of Sciences (GJHZ2063); National Natural Science Foundation of China (81773964, 82104497, 92068117, 81871809); Guangdong Youth Talent Support Program of Science and Technological Innovation (2017TQ04X885); Guangdong Basic and Applied Basic Research Fund (2020B1515120052); Shenzhen International Collaborative Project (GJHZ20190821160803823); Science and Technology Innovation Fund of Shenzhen (JCYJ20180302150101316, JCYJ20170818153602439); Sanming Project of Medicine in Shenzhen (SZSM201808072); Development and Reform Commission of Shenzhen Municipality (XMHT20190106001); Shenzhen Double Chain Project for Innovation and Development Industry supported by Bureau of Industry and Information Technology of Shenzhen (201908141541); Discipline construction project of Guangdong Medical University (4SG21002G).

Appendix A. Supplementary data

Supplementary data to this article can be found online at https://doi.org/10.1016/j.jot.2021.10.002.

References

[1] Raftery RM, Mencia Castano I, Chen G, Cavanagh B, Quinn B, Curtin CM, et al. Translating the role of osteogenic-angiogenic coupling in bone formation: highly efficient chitosan-pDNA activated scaffolds can accelerate bone regeneration in critical-sized bone defects. Biomaterials 2017;149:116–27.
[2] H. E., New method of applying autogenous intramedullary bone transplants and of making autogenous bone-screws. 1917.
[3] Augustin HG, Koh GY. Organotypic vasculature: from descriptive heterogeneity to functional pathophysiology. Science 2017;357(6353):eaal2379.
[4] Chandra P, Atala A. Engineering blood vessels and vascularized tissues: technology trends and potential clinical applications. Clin Sci 2019;133(9):1115–35.
[5] Hu K, Besschetnova TY, Olsen BR. Soluble VEGFR1 reverses BMP2 inhibition of intramembranous ossification during healing of cortical bone defects. J Orthop Res 2017;35(7):1461–9.
[6] Dreyer CH, Kjaergaard K, Ding M, Qin L. Vascular endothelial growth factor for in vivo bone formation: a systematic review. J Orthop Translat 2020;24:46–57.
[7] Bose S, Sarkar N. Natural medicinal compounds in bone tissue engineering. Trends Biotechnol 2020;38(4):404–17.
[8] Shang Y, Ma Y, Zhou Y, Zhang H, Duan L, Chen H, et al. Plant science. Biosynthesis, regulation, and domestication of bitterness in cucumber. Science 2014;346(6213):1084–8.
[9] Luo H, Vong CT, Chen H, Gao Y, Lyu P, Qiu L, et al. Naturally occurring anti-cancer compounds: shining from Chinese herbal medicine. Chin Med 2019;14:48.
[10] Ranjan A, Ramachandran S, Gupta N, Kaushik I, Wright S, Srivastava S, et al. Role of phytochemicals in cancer prevention. Int J Mol Sci 2019;20(20).
[11] Xue Y, Li R, Fang P, Ye ZQ, Zhao Y, Zhou Y, et al. NLRP3 inflammasome inhibitor cucurbitacin B suppresses gout arthritis in mice. J Mol Endocrinol 2021;67(2):27–40.
[12] Ma Y, Yoshida T, Matoba K, Kida K, Shintani R, Piao Y, et al. Identification of small compounds regulating the secretion of extracellular vesicles via a TIM4-affinity ELISA. Sci Rep 2021;11(1):13471.
[13] Qin L, Yao D, Zheng L, Liu WC, Liu Z, Lei M, et al. Phytomolecule icaritin incorporated PLGA/TCP scaffold for steroid-associated osteonecrosis: proof-of-concept for prevention of hip joint collapse in bipedal emus and mechanistic study in quadrupedal rabbits. Biomaterials 2015;59:125–43.
[14] Shi GS, Li YY, Luo YP, Jin JF, Sun YX, Zheng LZ, et al. Bioactive PLGA/tricalcium phosphate scaffolds incorporating phytomolecule icaritin developed for calvarial defect repair in rat model. J Orthop Translat 2020;24:112–20.
[15] Li L, Long J, Li L, Cao H, Tang T, Xi X, et al. Quantitative determination of residual 1,4-dioxane in three-dimensional printed bone scaffold. J Orthop Translat 2018;13:58–67.
[16] Lai Y, Cao H, Wang X, Chen S, Zhang M, Wang N, et al. Porous composite scaffold incorporating osteogenic phytomolecule icariin for promoting skeletal regeneration in challenging osteonecrotic bone in rabbits. Biomaterials 2018;153:1–13.
[17] Lai Y, Li Y, Cao H, Long J, Wang X, Li L, et al. Osteogenic magnesium incorporated into PLGA/TCP porous scaffold by 3D printing for repairing challenging bone defect. Biomaterials 2019;197:207–19.
[18] Chen D, Qin L, Yu X, Song G, Zhang P. Haemodialysis access via tissue-engineered vascular graft. Lancet 2009;374(9685).
[19] Spicer PP, Kretlow JD, Young S, Jansen JA, Kasper FK, Mikos AG. Evaluation of bone regeneration using the rat critical size calvarial defect. Nat Protoc 2012;7(10):1918–29.
[20] Zhu W, Chu C, Kuddannaya S, Yuan Y, Walczak P, Singh A, et al. In vivo imaging of composite hydrogel scaffold degradation using CEST MRI and two-color NIR imaging. Adv Funct Mater 2019;29(36).
[21] Young S, Patel ZS, Kretlow JD, Murphy MB, Mountziaris PM, Baggett LS, et al. Dose effect of dual delivery of vascular endothelial growth factor and bone morphogenetic protein-2 on bone regeneration in a rat critical-size defect model. Tissue Eng 2009;15(9):2347–62.
[22] Hussain H, Green IR, Saleem M, Khattak KF, Irshad M, Ali M. Cucurbitacins as anticancer agents: a patent review. Recent Pat Anti-Cancer Drug Discov 2019;14(2):133–43.
[23] Piao X-M, Gao F, Zhu J-X, Wang L-J, Zhao X, Li X, et al. Cucurbitacin B inhibits tumor angiogenesis by triggering the mitochondrial signaling pathway in endothelial cells. Int J Mol Med 2018;42(2):1018–25.
[24] Zhao D, Zhu T, Li J, Cui L, Zhang Z, Zhuang X, et al. Poly(lactic-co-glycolic acid)-based composite bone-substitute materials. Bioact Mater 2020;6(2):346–60.
[25] Zhu B, Xu W, Liu J, Ding J, Chen X. Osteoinductive agents-incorporated three-dimensional biphasic polymer scaffold for synergistic bone regeneration. ACS Biomater Sci Eng 2019;5(2):986–95.
[26] Bose S, Robertson SF, Bandyopadhyay A. Surface modification of biomaterials and biomedical devices using additive manufacturing. Acta Biomater 2018;66:6–22.
[27] Zhang B, Pei X, Song P, Sun H, Li H, Fan Y, et al. Porous bioceramics produced by inkjet 3D printing: effect of printing ink formulation on the ceramic macro and micro porous architectures control. Compos B Eng 2018;155:112–21.
[28] Chakkalakal DA, Mashoof AA, Novak J, Strates BS, McGuire MH. Mineralization and pH relationships in healing skeletal defects grafted with demineralized bone matrix. J Biomed Mater Res 1994;28(12):1439–43.
[29] Quintana RM, Jardine AP, Grechi TR, Grazziotin-Soares R, Ardenghi DM, Scarparo RK, et al. Bone tissue reaction, setting time, solubility, and pH of root repair materials. Clin Oral Invest 2019;23(3):1359–66.
[30] Hunsakunachai N, Nuengchamnong N, Jiratchariyakul W, Kummalue T, Khemawoot P. Pharmacokinetics of cucurbitacin B from Trichosanthes cucumerina L. in rats. BMC Compl Alternative Med 2019;19(1):157.
[31] Tomlinson RE, Silva MJ. HIF-1α regulates bone formation after osteogenic mechanical loading. Bone 2015;73:98–104.
[32] Stegen S, Laperre K, Eelen G, Rinaldi G, Fraisl P, Torrekens S, et al. HIF-1alpha metabolically controls collagen synthesis and modification in chondrocytes. Nature 2019;565(7740):511–5.
[33] Maes C, Carmeliet G, Schipani E. Hypoxia-driven pathways in bone development, regeneration and disease. Nat Rev Rheumatol 2012;8(6):358–66.
[34] Ramasamy SK, Kusumbe AP, Wang L, Adams RH. Endothelial Notch activity promotes angiogenesis and osteogenesis in bone. Nature 2014;507(7492):376–80.
[35] Xu R, Yallowitz A, Qin A, Wu Z, Shin DY, Kim J-M, et al. Targeting skeletal endothelium to ameliorate bone loss. Nat Med 2018;24(6):823–33.
[36] Apte RS, Chen DS, Ferrara N. VEGF in signaling and disease: beyond discovery and development. Cell 2019;176(6):1248–64.
[37] Ferrara N, Gerber H-P, LeCouter J. The biology of VEGF and its receptors. Nat Med 2003;9(6):669–76.
[38] Holmqvist K, Cross MJ, Rolny C, Hagerkvist R, Rahimi N, Matsumoto T, et al. The adaptor protein shb binds to tyrosine 1175 in vascular endothelial growth factor (VEGF) receptor-2 and regulates VEGF-dependent cellular migration. J Biol Chem 2004;279(21):22267–75.
[39] Simons M, Gordon E, Claesson-Welsh L. Mechanisms and regulation of endothelial VEGF receptor signalling. Nat Rev Mol Cell Biol 2016;17(10):611–25.
[40] Wang Y, Botvinick EL, Zhao Y, Berns MW, Usami S, Tsien RY, et al. Visualizing the mechanical activation of Src. Nature 2005;434(7036):1040–5.

[41] Anderson D, Koch CA, Grey L, Ellis C, Moran MF, Pawson T. Binding of SH2 domains of phospholipase C gamma 1, GAP, and Src to activated growth factor receptors. Science (New York, N.Y.) 1990;250(4983):979–82.
[42] Tavora B, Reynolds LE, Batista S, Demircioglu F, Fernandez I, Lechertier T, et al. Endothelial-cell FAK targeting sensitizes tumours to DNA-damaging therapy. Nature 2014;514(7520):112–6.
[43] Fulton D, Gratton JP, McCabe TJ, Fontana J, Fujio Y, Walsh K, et al. Regulation of endothelium-derived nitric oxide production by the protein kinase Akt. Nature 1999;399(6736):597–601.
[44] Lopes D, Martins-Cruz C, Oliveira MB, Mano JF. Bone physiology as inspiration for tissue regenerative therapies. Biomaterials 2018;185:240–75.
[45] Chen R, Wang J, Liu C. Biomaterials act as enhancers of growth factors in bone regeneration. Adv Funct Mater 2016;26(48):8810–23.
[46] Zhu T, Cui Y, Zhang M, Zhao D, Liu G, Ding J. Engineered three-dimensional scaffolds for enhanced bone regeneration in osteonecrosis. Bioact Mater 2020;5(3):584–601.
[47] Okesola BO, Ni S, Derkus B, Galeano CC, Hasan A, Wu Y, et al. Growth-factor free multicomponent nanocomposite hydrogels that stimulate bone formation. Adv Funct Mater 2020;30(14):1906205.